*J. Fluid Mech.* (1999), *vol.* 380, *pp.* 141–168. Printed in the United Kingdom



# Receptivity to surface roughness near a swept leading edge

By S. SCOTT COLLIS[1]† AND SANJIVA K. LELE[2]

[1]Rice University, MS 321, Houston, TX 77005-1892, USA
[2]Stanford University, Stanford, CA 64305-4035, USA

(Received 2 June 1997 and in revised form 14 August 1998)

The formation of stationary crossflow vortices in a three-dimensional boundary layer due to surface roughness located near the leading edge of a swept wing is investigated using numerical solutions of the compressible Navier–Stokes equations. The numerical solutions are used to evaluate the accuracy of theoretical receptivity predictions which are based on the parallel-flow approximation. By reformulating the receptivity theory to include the effect of surface curvature, it is shown that convex surface curvature enhances receptivity. Comparisons of the parallel-flow predictions with Navier–Stokes solutions demonstrate that non-parallel effects strongly reduce the initial amplitude of stationary crossflow vortices. The curvature and non-parallel effects tend to counteract one another; but, for the cases considered here, the non-parallel effect dominates leading to significant over-prediction of receptivity by parallel-flow receptivity theory. We conclude from these results that receptivity theories must account for non-parallel effects in order to accurately predict the amplitude of stationary crossflow instability waves near the leading edge of a swept wing.

## 1. Introduction

Laminar-flow wings show promise for reducing viscous drag forces in cruise for commercial aircraft. However, the success of a laminar-flow wing depends critically on the external disturbance environment and how these disturbances influence the transition from laminar to turbulent flow. The process by which external disturbances are converted into instability waves, which are the precursors to turbulence, is called receptivity (Morkovin 1969).

In wing design, current transition prediction techniques rely on the $e^N$ method (Malik 1990) in which an amplitude ratio, predicted by local linear-stability theory, is correlated with the transition location. The success of this technique is hampered by the assumptions of linearity and (usually) parallel flow, and by the exclusion of the receptivity process which determines the initial amplitude of disturbances within the boundary layer. Although the $e^N$ method is successful in predicting the transition for two-dimensional disturbances (i.e. Tollmien–Schlichting waves) it has been found to be highly unreliable when streamwise disturbances are present. The fundamental assumptions of the $e^N$ method are particularly questionable immediately downstream of the attachment line on a swept wing where the mean boundary layer is very thin and rapidly growing. Here, the flow is highly sensitive to surface roughness (Braslow *et al.* 1990; Reibert *et al.* 1996) which can take a variety of forms in practice: manufacturing

† Formerly at Stanford University.

defects, insect debris, ice crystals, etc. Recent experiments by Reibert *et al.* (1996) and Deyhle & Bippes (1996) demonstrate that surface roughness is the primary cause of stationary crossflow vortices and that stationary vortices dominate the transition process near the leading edge of swept wings in low-disturbance environments – such as the cruise condition for an aircraft in flight. However, it must be noted that travelling crossflow instability waves are also unstable under flight conditions and may be important to the transition process depending on the disturbance environment.

Recently, the linear and early nonlinear evolution of crossflow vortices has been well-predicted by analysis based on the Parabolized Stability Equations (PSE) (Haynes & Reed 1996; Malik, Li & Chang 1994) and these equations form the starting point for an amplitude-based transition prediction criterion, proposed by Herbert (1991), to replace $e^N$ methods. Transition prediction based on PSE naturally incorporates non-parallel and nonlinear effects and fully accounts for both two- and three-dimensional instability mechanisms. A complete amplitude-based transition criterion requires the ability to predict the receptivity of the boundary layer to external disturbances. However, the receptivity process for crossflow modes remains an open issue mainly because experimental studies of receptivity due to surface roughness are hampered by several factors: (i) the complete disturbance environment is generally unknown, (ii) the amplitudes of crossflow instability waves near the source of receptivity are not measurable, and (iii) at downstream stations where measurements are possible, nonlinear effects may have already occurred. Through the numerical simulations presented here, each of these limitations is overcome and results are obtained that are used to evaluate theoretical receptivity predictions. The evaluation and enhancement of theoretical approaches is of critical importance, since theoretical predictions will probably be the means of incorporating receptivity into an improved transition prediction methodology for laminar-flow-wing design.

There has been considerable theoretical research on the prediction of receptivity in three-dimensional boundary layers. A useful review article is given by Choudhari & Streett (1990) in which the different receptivity mechanisms for the generation of stationary and travelling crossflow modes are discussed. In particular, it is suggested that although the travelling crossflow instability modes have larger linear growth rates than stationary modes, local receptivity mechanisms preferentially excite stationary modes. This hypothesis has been recently verified by Crouch (1993) and Choudhari (1994) who have independently studied the receptivity of crossflow modes for incompressible flow where the mean boundary layer is given by the family of Falkner–Skan–Cooke (Cooke 1950) swept-wedge flows. The analysis used by both Crouch (1993) and Choudhari (1994) is done in the same framework as the classical asymptotic receptivity theories of Goldstein (1985) and Ruban (1984). However, instead of approximating the Navier–Stokes equations using high Reynolds number expansions, the equations are replaced by the locally parallel equations in the vicinity of the surface disturbance. This approach was first used by Zavol'skii, Reutov & Ryboushkina (1983) to study the generation of Tollmien–Schlichting waves in the boundary layer over a wavy surface and several recent review articles (Choudhari & Streett 1994; Crouch 1994) summarize the various applications of this technique. The advantage of what has been called Finite Reynolds Number Theory (FRNT) is that solutions can be more easily obtained for a wide range of physical problems at moderate Reynolds numbers. Furthermore, FRNT is not limited to the vicinity of the first neutral point as is the asymptotic theory. Using FRNT, Crouch (1993) and Choudhari (1994) demonstrate that the initial amplitudes of travelling crossflow modes due to the interaction of free-stream acoustic waves with surface roughness

is much smaller than that of stationary modes which are generated by the direct scattering of the mean flow by the roughness. This conclusion is directly related to the fact that the amplitude of unsteady free-stream disturbances (both sound and turbulence) is very low under flight conditions and this conclusion is consistent with the experimental observations of Radeztsky, Reibert & Saric (1993) and Deyhle & Bippes (1996). Also consistent with the experimental results, the theory predicts the greatest crossflow instability wave amplitude to occur for roughness just upstream of the first neutral point. Although receptivity actually increases upstream of the neutral point, the amplitude of a generated instability wave in the unstable region is reduced because disturbances are highly damped upstream of the neutral point. However, as pointed out by Choudhari (1994), the results of the theoretical predictions require numerical and/or experimental verification in the vicinity of the first neutral point because non-parallel effects may be important. Additionally, in practical situations, such as the leading edge of a swept wing, the first neutral point for stationary crossflow vortices will occur in a region of large surface curvature.

The effects of both non-parallel flow and surface curvature on the stability characteristics of stationary crossflow vortices have been recently examined by Malik and coworkers (Masad & Malik 1994; Malik & Balakumar 1993; Malik & Li 1993) using both PSE and perturbation theory to account for the non-parallel effects in the boundary layer on a swept circular cylinder. These results have generally shown that convex curvature is stabilizing while non-parallel effects are destabilizing for crossflow modes. However, the impact of non-parallelism and curvature remain open issues with regard to receptivity.

Given the importance of stationary crossflow vortices in the transition process on swept wings, the mechanisms responsible for their formation and the accurate prediction of their initial amplitude are essential for the development of practical laminar-flow wings. The results presented here close the gap in transition prediction by determining the receptivity of crossflow vortices through numerical simulation of the Navier–Stokes equations. In this way, the disturbance environment can be carefully controlled and both the physical mechanisms of the receptivity process and the success and limitations of the theoretical approaches (Choudhari 1994; Crouch 1993) can be established. In particular, the effects of both body curvature and non-parallel mean flow are examined in the context of a simplified model of a wing leading edge and the results are used to evaluate receptivity predictions based on finite Reynolds number theory.

The discussion begins in § 2 with the problem formulation and solution techniques followed by a comparison of results from receptivity calculations and theoretical receptivity predictions in § 3. Finally the major findings and conclusions of this study are summarized in § 4.

## 2. Formulation

In this section, the receptivity problem and governing equations are described, followed by a summary of the numerical methods used to obtain Navier–Stokes-based receptivity solutions. The section ends with a brief synopsis of the linear stability and receptivity theories used for comparison to the Navier–Stokes results.

### 2.1. *Problem description and governing equations*

The parabolic cylinder, shown in figure 1, is used to model the leading edge of a swept wing. The parabolic cylinder is an ideal geometry for the investigation of

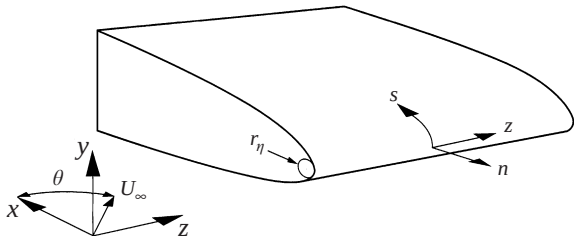


FIGURE 1. Swept parabolic-cylinder geometry.

crossflow instability and receptivity due to the extended region of favourable pressure gradient which drives the crossflow instability. In addition, the boundary layer over the parabolic cylinder naturally approaches a Blasius-like profile far downstream, since the surface curvature and pressure gradient naturally decay downstream. Likewise, non-parallel effects due to the rapidly growing boundary layer near the leading edge are also attenuated downstream. Thus, progressing downstream of the leading edge, the stability and receptivity characteristics will be increasingly well-predicted by parallel, flat-plate theory, providing a reference for the comparison of numerical and theoretical results. From a practical perspective, the parabolic cylinder is a convenient geometry since it is described by a simple analytical function and a conformal transformation exists which maps the parabolic cylinder to a flat plate (Van Dyke 1963).

To create a three-dimensional boundary layer, the parabolic cylinder is swept at an angle $\theta$ with respect to a uniform incoming flow with velocity magnitude $U_\infty$. Two coordinate systems are shown in figure 1. Velocity components in the global coordinates are denoted by $u$ in the chordwise ($x$) direction, $v$ in the vertical ($y$) direction, and $w$ in the spanwise ($z$) direction. In the body-fixed coordinate system, the arc-length along the surface of the wing is given by $s$, the distance normal to the wing surface is $n$, and $z$ is again the spanwise direction. Velocity components in this coordinate system are denoted by $v_s$, $v_n$, and $w$ for the $s$-, $n$-, and $z$-directions, respectively. The parabolic cylinder is at zero angle of attack relative to the free-stream velocity and is idealized as having infinite span with no taper. This avoids end effects and renders all $z$-derivatives zero in the mean.

The natural length scale for the parabolic cylinder is the leading-edge radius, $r_n^*$, where the superscript $*$ denotes dimensional quantities. In the following, all lengths are non-dimensionalized using $r_n^*$ and velocities are non-dimensionalized using the chordwise component of the free-stream velocity, $u_\infty^* = U_\infty^* \cos(\theta)$. The reference time scale is the free-stream convective scale, $r_n^*/u_\infty^*$, and temperature and density are non-dimensionalized using their free-stream values, $T_\infty^*$ and $\rho_\infty^*$, respectively. The reference pressure is then given by twice the free-stream dynamic pressure, $\rho_\infty^*(u_\infty^*)^2$.

The flow over a swept parabolic cylinder is modelled using an ideal gas where both the specific heat at constant pressure, $c_p^*$, and the specific heat at constant volume, $c_v^*$, are constant. The dynamic viscosity, $\mu^*$, is also held constant and Stokes' hypothesis is used to compute the second coefficient of viscosity. A unit Prandtl number, $Pr = \mu^* c_p^*/\kappa^* = 1$, is assumed where $\kappa^*$ is the thermal conductivity and the ratio of specific heats, $\gamma = c_p{}^*/c_v{}^*$, is 1.4. The use of constant specific heats, viscosities, and Prandtl number is not expected to have a qualitative effect on receptivity or stability, in the flow regime studied here, but does greatly simplify the current analysis.

Under these conditions, the flow is governed by the following non-dimensional form of the compressible Navier–Stokes equations, written using coordinate-system-independent vector notation

$$\frac{\partial \rho}{\partial t} + \nabla \cdot (\rho \boldsymbol{u}) = 0, \tag{2.1a}$$

$$\rho \left( \frac{\partial \boldsymbol{u}}{\partial t} + \boldsymbol{u} \cdot \nabla \boldsymbol{u} \right) = -\nabla p + \frac{2}{Re} \left[ \nabla \cdot \boldsymbol{S} - \tfrac{1}{3} \nabla (\nabla \cdot \boldsymbol{u}) \right], \tag{2.1b}$$

$$\rho \frac{\partial T}{\partial t} + \rho \boldsymbol{u} \cdot \nabla T + (\gamma - 1) \rho T \nabla \cdot \boldsymbol{u} = \frac{\gamma}{Re} \nabla^2 T + \frac{2\gamma(\gamma - 1) M^2}{Re} \left[ \boldsymbol{S} \cdot \boldsymbol{S} - \tfrac{1}{3} (\nabla \cdot \boldsymbol{u})^2 \right], \tag{2.1c}$$

where $\boldsymbol{S}$ is the strain-rate tensor, $\boldsymbol{u}$ is the velocity vector, $\nabla$ is the gradient operator, and the pressure is given by the equation of state

$$p = \rho T / (\gamma M^2). \tag{2.1d}$$

In these equations, the Mach number is defined as $M = u^*_\infty / c^*_\infty$, where $c^*_\infty$ is the free-stream speed of sound, and the Reynolds number is $Re = \rho^*_\infty u^*_\infty r^*_n / \mu^*$.

The parameters for the numerical simulations are selected to generate a flow which roughly models the flow near the leading edge of a subsonic transport aircraft in cruise. For this purpose, we use a sweep angle of $\theta = 35^\circ$ with $M = 0.8$ and $Re = 1 \times 10^5$. It should be emphasized that these conditions only approximate the flow of air around an aircraft wing, since unit Prandtl number and constant fluid properties are assumed. In the free-stream, the Mach number is defined as $M_\infty = U_\infty / c_\infty = M(1 + \tan^2(\theta))^{1/2}$ and for the conditions used here, $M_\infty = 0.98$. Assuming that the nose radius of a typical airfoil section is approximately 1% chord (Abbott & von Doenhoff 1959), these conditions correspond to a chord Reynolds number of $1 \times 10^7$ which is in the realm of flight Reynolds numbers.

Here, we consider the linear receptivity of the three-dimensional boundary layer on the swept parabolic cylinder. The flow variables are written as

$$\rho = \bar{\rho}(\boldsymbol{x}) + \varepsilon_w \, \rho'(\boldsymbol{x}, t), \quad \boldsymbol{u} = \bar{\boldsymbol{u}}(\boldsymbol{x}) + \varepsilon_w \, \boldsymbol{u}'(\boldsymbol{x}, t), \tag{2.2a,b}$$

$$T = \bar{T}(\boldsymbol{x}) + \varepsilon_w \, T'(\boldsymbol{x}, t), \quad p = \bar{p}(\boldsymbol{x}) + \varepsilon_w \, p'(\boldsymbol{x}, t), \tag{2.2c,d}$$

where a bar denotes base-flow variables; primes denote linear perturbations about that base flow; and $\varepsilon_w$ represents the non-dimensional surface roughness height, $\varepsilon_w = \varepsilon^*_w / r^*_n \ll 1$. Although the current work addresses stationary disturbances, we allow for unsteady perturbations since a time-marching scheme is used to find the steady disturbance solution.

Substituting (2.2) into (2.1) and dropping terms that are nonlinear in $\varepsilon_w$ leads to two sets of equations: one for the base flow and one for the perturbation flow. The base flow equations are just the steady version of (2.1). The perturbation equations, referred to here as the Linearized Navier–Stokes (LNS) equations, are given by

$$\frac{\partial \rho'}{\partial t} + \nabla \bar{\rho} \cdot \boldsymbol{u}' + \nabla \rho' \cdot \bar{\boldsymbol{u}} + \bar{\rho} \nabla \cdot \boldsymbol{u}' + \rho' \nabla \cdot \bar{\boldsymbol{u}} = 0, \tag{2.3a}$$

$$\bar{\rho} \frac{\partial \boldsymbol{u}'}{\partial t} + \rho' (\bar{\boldsymbol{u}} \cdot \nabla) \bar{\boldsymbol{u}} + \bar{\rho} (\boldsymbol{u}' \cdot \nabla) \bar{\boldsymbol{u}} + \bar{\rho} (\bar{\boldsymbol{u}} \cdot \nabla) \boldsymbol{u}' = -\nabla p' + \frac{2}{Re} \left[ \nabla \cdot \boldsymbol{S}' - \tfrac{1}{3} \nabla (\nabla \cdot \boldsymbol{u}') \right], \tag{2.3b}$$

$$\bar{\rho}\frac{\partial T'}{\partial t} + \rho'(\bar{\boldsymbol{u}}\cdot\nabla)\bar{T} + \bar{\rho}(\boldsymbol{u}'\cdot\nabla)\bar{T} + \bar{\rho}(\bar{\boldsymbol{u}}\cdot\nabla)T' + (\gamma-1)\left[\bar{\rho}\bar{T}\nabla\cdot\boldsymbol{u}' + \bar{\rho}T'\nabla\cdot\bar{\boldsymbol{u}} + \rho'\bar{T}\nabla\cdot\bar{\boldsymbol{u}}\right] = \frac{\gamma}{Re}\nabla^2 T' + \frac{4\gamma(\gamma-1)M^2}{Re}\left[\bar{\boldsymbol{S}}\cdot\boldsymbol{S}' - \tfrac{1}{3}(\nabla\cdot\bar{\boldsymbol{u}})\nabla\cdot\boldsymbol{u}'\right], \tag{2.3c}$$

where the linearized equation of state is

$$p' = (\bar{\rho}T' + \bar{T}\rho')/(\gamma M^2). \tag{2.3d}$$

The LNS equations can be written in the compact form

$$\frac{\partial \boldsymbol{U}'}{\partial t} + \mathbf{L}(\boldsymbol{U}';\bar{\boldsymbol{U}}) = \mathbf{0}, \tag{2.4}$$

where the vector of primitive variables is $\boldsymbol{U} = \{\rho, \boldsymbol{u}^{\mathrm{T}}, T\}^{\mathrm{T}}$ and $\mathbf{L}(\boldsymbol{U}';\bar{\boldsymbol{U}})$ is a linear operator which depends on the base flow and acts on the disturbance variables.

The general procedure for solving the surface roughness receptivity problem is as follows. First, the steady Navier–Stokes equations, subject to appropriate boundary conditions (see § 2.2), are solved to obtain the base-flow about the swept parabolic cylinder. Then, (2.4) is solved subject to boundary conditions (see § 2.3) which include surface roughness. The solution to (2.4) represents the response of the boundary layer to the surface roughness disturbance and, from this solution, the initial amplitude of the dominant crossflow instability wave is extracted (see § 3.3) to determine receptivity.

### 2.2. *Numerical approach for base-flow solutions*

This section summarizes the numerical method used to obtain the base-flow solution about the swept parabolic cylinder. For additional information about mesh generation, discretization, and boundary treatments, the reader is referred to Collis (1997). Figure 2 shows the computational domain and mesh used to obtain the base flow about the parabolic cylinder. This mesh is constructed using the conformal mapping of the parabolic cylinder to a flat plate with additional mapping functions used to cluster points near the leading edge and in the boundary layer. Taking advantage of symmetry about the $x$-axis, the computational domain is limited to the upper half of the flow field. An isothermal, no-slip boundary condition is enforced on the surface of the parabolic cylinder. Thus, the wall velocities are given by

$$\bar{\boldsymbol{u}}(s,0) = 0 \tag{2.5}$$

and the wall temperature is set to the free-stream stagnation temperature, $T_0$,

$$\bar{T}(s,0) = T_0 \equiv 1 + \frac{\gamma-1}{2}M_\infty^2 \tag{2.6}$$

which is also the adiabatic wall temperature since we use $Pr = 1.0$. On the inflow boundary, the incoming Riemann invariants are enforced based on a potential flow solution and outgoing Riemann invariants are extrapolated from the interior of the computational domain. On the outflow boundary, a boundary treatment based on the parabolized Navier–Stokes equations has been developed which allows the viscous boundary layer to smoothly leave the computational domain with very little upstream influence (Collis 1997).

With these boundary conditions, (2.1 *a–c*) are first converted to a generalized coordinate system in order to map the mesh shown in figure 2 to a uniform computational

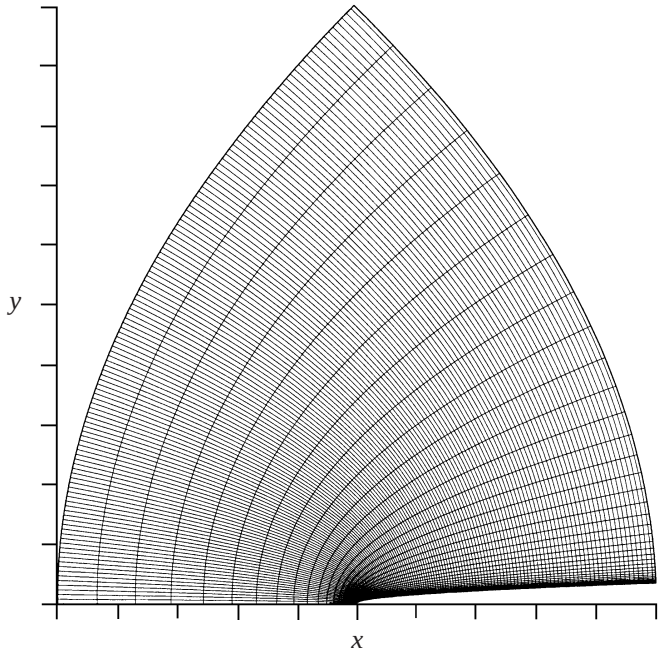


FIGURE 2. Parabolic cylinder mesh for base-flow computation, every third mesh line shown for clarity. Tic marks denote $100r_n^*$.

domain. In the uniform computational space, fourth-order-accurate central differences are used for all interior spatial derivatives. Near the computational boundaries, one-sided differences are used which ensure overall fourth-order accuracy. Since the parabolic cylinder is assumed to have infinite span, all $z$-derivatives are zero so that the base-flow solution is two-dimensional in the $(x, y)$-plane, but with three non-zero components of velocity due to wing sweep. The discretized equations are marched to the steady state using the fully-implicit, first-order-accurate, backward Euler time-advancement scheme. Convergence to the steady state is accelerated by using local time stepping. To solve the nonlinear system of equations at each time step, a Newton iteration is employed along with approximate factorization of the Jacobian to economically solve the large system of linear equations at each iteration. This results in a series of block (nearly, but spoiled by the boundary nodes) penta-diagonal systems of equations which are solved at each iteration using a specially developed LU decomposition routine optimized for vector supercomputers. Typically, only one Newton iteration is used per time step, since time accuracy is not required.

To validate our numerical approach, base-flow solutions for an unswept parabolic cylinder, obtained with the current method, were compared to the reference incompressible solutions of Davis (1972). These comparisons are reported in Collis (1997) and when extrapolated to zero Mach number, the solutions using the current method are in excellent agreement with Davis (1972).

### 2.3. *Numerical approach for receptivity solutions*

With the base-flow solution known, the receptivity to surface roughness of the three-dimensional boundary layer on the swept parabolic cylinder is investigated by solving (2.4) in the vicinity of the roughness location. Figure 3 shows a schematic

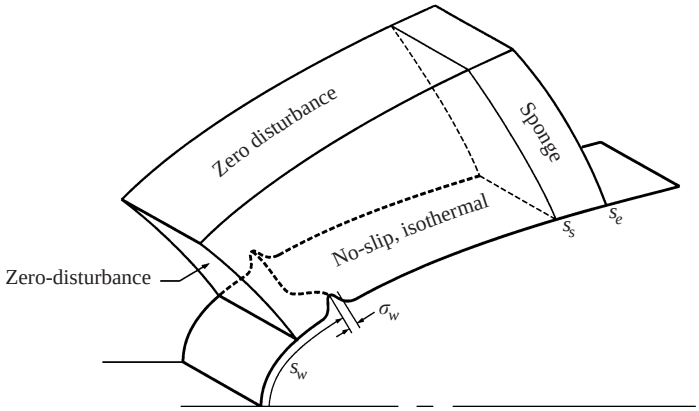


FIGURE 3. Schematic of computational domain for a receptivity calculation showing the surface roughness geometry.

of the computational domain including boundary conditions used for the linearized calculations.

Without loss of generality, the surface roughness is modelled by a single Fourier mode in the spanwise direction. Under the linear assumption, more complicated spanwise distributions can be constructed as a superposition of the individual spanwise Fourier modes. Thus, denoting the smooth wall by $n(s,z) = 0$ the rough wall is obtained by adding a small, spanwise-periodic perturbation given by

$$n'(s,z) = \varepsilon_w h_w(s) \mathrm{e}^{\mathrm{i}k_z z}, \tag{2.7}$$

where $h_w(s)$ is the chordwise shape of the roughness, $k_z = k_z^* r_n^*$ is the spanwise wavenumber of the roughness, and the real-part convention is used. For the cases presented here, a Gaussian distribution,

$$h_w(s) = \exp\left[\frac{-(s-s_w)^2}{2\sigma_w^2}\right], \tag{2.8}$$

is used for the chordwise roughness shape, where the roughness is centred about $s_w$ and $\sigma_w$ is the standard deviation (i.e. measure of the width) of the Gaussian distribution. In computing theoretical receptivity predictions, the Fourier transform of the bump is required in the chordwise direction. For a Gaussian distribution, the Fourier transform is also Gaussian and is given by

$$\hat{h}_w(k_s) = \sigma_w \exp\left[\frac{-k_s^2\sigma_w^2}{2}\right], \tag{2.9}$$

where $k_s$ is the wavenumber in the $s$-direction.

No-slip, isothermal boundary conditions are imposed on the disturbed wall. Under the linear assumption, the boundary conditions on the rough wall can be transferred by a Taylor series expansion to inhomogeneous boundary conditions on the undisturbed surface (Collis 1997). This results in the following wall boundary conditions for the disturbance variables:

$$\boldsymbol{u}'(s,0,z) = -h_w(s)\mathrm{e}^{\mathrm{i}k_z z}\frac{\partial \bar{\boldsymbol{u}}}{\partial n}(s,0), \tag{2.10}$$

$$T'(s,0,z) = -h_w(s)\mathrm{e}^{\mathrm{i}k_z z}\frac{\partial \bar{T}}{\partial n}(s,0). \tag{2.11}$$

For receptivity calculations, the inflow boundary is placed at least $4\sigma_w$ upstream of the roughness location which allows the use of zero disturbance boundary conditions. Similarly, the top boundary is located at least eight boundary layer thicknesses above the parabolic cylinder, at the outflow boundary, which again allows zero disturbance boundary conditions to be used. The accuracy and viability of these boundary conditions and locations were determined by performing a calculation for a larger domain which showed no significant change in the boundary layer response.

Near the outflow boundary, a sponge term (Israeli & Orszag 1981) is added to the right-hand side of (2.4),

$$\boldsymbol{F}_s = f_s(s)\boldsymbol{U}'(s,n,z), \tag{2.12}$$

where $f_s(s)$ is the sponge function which is designed to vary smoothly from zero in the interior to a finite value, $A_s$, on the boundary. For this purpose, we use the cubic function

$$f_s(s) = \begin{cases} A_s\left(\dfrac{s-s_s}{s_e-s_s}\right)^3, & s \in (s_s, s_e] \\ 0, & \text{otherwise.} \end{cases} \tag{2.13}$$

In this expression, $s_s$ denotes the start of the sponge and $s_e$ the end. For all calculations presented here, $s_e$ corresponds to the end of the computational domain, $s_s = 0.8s_e$, and $A_s = 80$. Extensive testing and validation of the outflow sponge has been performed for crossflow instability waves (Collis 1997). From this investigation, an outflow sponge region with streamwise length of at least one wavelength of the crossflow instability wave was found sufficient to reduce reflections to less than 0.3%, when measured using the error in the spatial growth rate. For all cases presented here, the sponge region described above is at least one instability wavelength long and no reflections where observed.

Given the base-flow solution and disturbance boundary conditions, the disturbance solution is written as

$$\boldsymbol{U}'(x,y,z,t) = \hat{\boldsymbol{U}}(x,y,t)\,\mathrm{e}^{\mathrm{i}k_z z}, \tag{2.14}$$

where the real-part convention is used. This expression is substituted into (2.4) and the resulting system of equations is converted to a generalized coordinate system in the $(x, y)$-plane which enables the physical mesh to be mapped to a uniform computational domain. The same fourth-order spatial discretization used for the base-flow solver § 2.2 is used here in the computational domain. Since we are interested in steady surface disturbances, the discretized equations are marched to the steady-state solution again using the backward Euler time-advancement scheme. Approximate factorization is used to reduce the large (complex) system of linear equations into a series of block (nearly) penta-diagonal systems of equations which are solved using an optimized LU decomposition routine. Additional details of the numerical method along with extensive validation can be found in Collis (1997).

### 2.4. *Linear stability theory*

The solution of the linearized Navier–Stokes equations, as described in (§ 2.3), gives the exact linear receptivity and stability characteristics including the effects of surface curvature and non-parallel flow. For comparison, we also solve the linear stability equations in the body-fitted orthogonal coordinate system, $(s, n, z)$, with a perturbation approach to account for non-parallel effects. We start with (2.4) where the velocity vector takes the form $\boldsymbol{u} = \{v_s, v_n, w\}^{\mathrm{T}}$ and differential distances in the $s$-direction are given by $h(s,n)\mathrm{d}s$ where $h(s,n)$ is the coordinate system metric and metrics in the

other coordinate directions are unity. Each of the differential operators in (2.4) can be written as a combination of partial derivatives with respect to $(s, n, z)$ and additional terms involving the metric and its derivatives. The generalized, differential operators required for the Navier–Stokes equations can be found in basic texts such as Sherman (1990). The detailed form of the equations for the body-fitted coordinate system is given in Collis (1997) along with a more thorough discussion of the stability theory and solution methodology.

Nonparallel stability characteristics are determined using a perturbation approach, pioneered by Ling & Reynolds (1973) and Saric & Nayfeh (1975). For high Reynolds numbers, the mean boundary layer flow, $\bar{\boldsymbol{U}}$, can be considered a slowly varying function of the streamwise coordinate, $s$. Defining a slow coordinate, $s_1 = \varepsilon s$, the base flow is written as an expansion in the parameter $\varepsilon$

$$\bar{\boldsymbol{U}}(s, n) = \bar{\boldsymbol{U}}_0(s_1, n) + \varepsilon \bar{\boldsymbol{U}}_1(s_1, n) + \ldots, \tag{2.15}$$

where $\varepsilon$ is a small dimensionless parameter representing the non-parallelism of the base flow. Here, $\bar{\boldsymbol{U}}_0(s_1, n)$ is the quasi-parallel base flow, and $\bar{\boldsymbol{U}}_1(s_1, n)$ is the first-order non-parallel correction which, for the class of flows considered here, consists only of the scaled, wall-normal velocity, $\bar{\boldsymbol{U}}_1 = \{0, 0, \bar{v}_n/\varepsilon, 0, 0\}^{\mathrm{T}}$.

Utilizing the method of multiple scales, linear disturbances about the base flow can be expanded in $\varepsilon$ as

$$\boldsymbol{U}'(s, n, z, t) = \left\{ A(s_1)\hat{\boldsymbol{U}}_0(s_1, n) + \varepsilon \hat{\boldsymbol{U}}_1(s_1, n) + \ldots \right\} \times \exp\left( \int \mathrm{i}k_s(s_1)\mathrm{d}s + \mathrm{i}k_z z - \mathrm{i}\omega t \right), \tag{2.16}$$

where $k_s$ is the chordwise wavenumber, $k_z$ is the spanwise wavenumber, and $\omega$ is the angular frequency. From the following analysis $\hat{\boldsymbol{U}}_0(s_1, n)$ will be identified as the quasi-parallel eigenfunction, $A(s_1)$ as the local wave amplitude, and $\hat{\boldsymbol{U}}_1(s_1, n)$ as the non-parallel correction at $O(\varepsilon)$.

Equations (2.15) and (2.16) are substituted into (2.4) and terms are grouped in powers of $\varepsilon$. At $O(\varepsilon^0)$ we obtain the parallel, linear stability equations

$$\mathbf{L}_0(\hat{\boldsymbol{U}}_0; k_s, k_z, \omega) = 0 \tag{2.17}$$

which are solved subject to homogeneous boundary conditions leading to an eigenvalue problem for $(k_s, \hat{\boldsymbol{U}}_0)$ given $k_z$.

At $O(\varepsilon^1)$ we obtain an equation of the form

$$\mathbf{L}_0(\hat{\boldsymbol{U}}_1; k_s, k_z, \omega) = \boldsymbol{G}\frac{\mathrm{d}A}{\mathrm{d}s_1} + \boldsymbol{H}A, \tag{2.18}$$

where $\boldsymbol{G}$ and $\boldsymbol{H}$ depend on $k_s$ and the non-parallel mean-flow terms, $\bar{\boldsymbol{U}}_1$. Equation (2.18) is subject to the same homogeneous boundary conditions as (2.17) and for a solution to exist, a solvability condition must be satisfied. This is accomplished by introducing the adjoint eigenfunction and requiring that the solution to (2.18) be orthogonal to the null space of $\mathbf{L}_0$. The details of this procedure, including the determination of the adjoint eigenfunction from the adjoint equation, are given in Collis (1997) but for our purposes here, it is sufficient to say that enforcing the solvability condition leads to, at lowest order, a solution of the form

$$\boldsymbol{U}'(s, n, z, t) = A(s_0)\hat{\boldsymbol{U}}_0(s, n)\, \exp\left[ \int_{s_0}^{s} \left( \mathrm{i}k_s(s) - \tilde{k}_s(s) \right) \mathrm{d}s + \mathrm{i}k_z z - \mathrm{i}\omega t \right], \tag{2.19}$$

where $s_0$ is an arbitrary reference location and $\tilde{k}_s$ is the non-parallel mean-flow term which results from enforcing the solvability condition. From this form of the solution, the spatial growth rate, $\sigma$, and real component of the chordwise wavenumber, $\alpha$, are given by

$$\sigma = -\mathrm{Im}(k_s) - \mathrm{Re}(\tilde{k}_s) + \mathrm{Re}\left(\frac{\partial}{\partial s}\ln(\hat{U}_0)\right), \tag{2.20a}$$

$$\alpha = \mathrm{Re}(k_s) - \mathrm{Im}\left(\tilde{k}_s\right) + \mathrm{Im}\left(\frac{\partial}{\partial s}\ln(\hat{U}_0)\right). \tag{2.20b}$$

The three terms which contribute to the non-parallel growth rate in (2.20*a*) are, in order of appearance: the quasi-parallel growth rate with curvature, the non-parallel mean-flow term, and the eigenfunction growth term. Note that $\hat{U}_0$ is any quantity based on the quasi-parallel eigenfunction and can be a function of both $s$ and $n$. In general, both $\sigma$ and $\alpha$ depend on the particular disturbance quantity used and on the wall-normal coordinate. To avoid ambiguity, all growth-rate results are presented in terms of the square-root of the integrated disturbance kinetic energy

$$\hat{K} \equiv \left[\frac{1}{2}\int_0^\infty (\hat{\boldsymbol{u}}\cdot\hat{\boldsymbol{u}})\,\mathrm{d}n\right]^{1/2} \tag{2.21}$$

which removes the $n$ dependence of the growth rate. Thus, in equation (2.20*a*), $\hat{U}_0$ is replaced by $\hat{K}_0$. Since there is no phase information in $\hat{K}$, $\alpha$ in (2.20*b*) is computed using $\hat{U}_0 = \hat{v}_{s0}$ at the point where $|\hat{v}_{s0}|$ is a maximum in $n$.

In practice, the quasi-parallel eigenproblem (2.17) is solved using Chebyshev collocation with a matrix eigenvalue solver. To enforce the solvability condition, the adjoint equation is solved using fourth-order Runge–Kutta integration with orthonormalization (Conte 1966). The reader is referred to Collis (1997) for additional details.

### 2.5. *Parallel-flow receptivity theory*

Receptivity results from the linearized Navier–Stokes solutions are compared to theoretical receptivity predictions obtained using Finite Reynolds Number Theory (FRNT). The development of the theory follows the exposition given by Choudhari (1994) with appropriate extensions to include compressibility and surface curvature (Collis 1997).

In FRNT, the linearized Navier–Stokes equations are approximated by the quasi-parallel disturbance equations. Consistent with this, the solution is expanded as

$$\boldsymbol{U}(S,n,z) = \bar{\boldsymbol{U}}(s_w,n) + \varepsilon_w \boldsymbol{U}'(S,n,z) + \ldots, \tag{2.22}$$

where the two-dimensional base flow in (2.2) has been replaced with the local quasi-parallel approximation at $s_w$ and we have introduced the shifted streamwise coordinate, $S = s - s_w$. Formally, this approximation is only valid when the Reynolds number based on $s_w$ is large (see Choudhari 1994). The disturbance $\boldsymbol{U}'$ is obtained by solving the Navier–Stokes equations linearized about the parallel base flow

$$\mathbf{L}(\boldsymbol{U}';\bar{\boldsymbol{U}}(s_w,n)) = \mathbf{0} \tag{2.23}$$

subject to the wall boundary conditions (2.10) and homogeneous boundary conditions as $n \to \infty$. Since the mean flow is parallel, the solution can be expanded in a Fourier series, which, when substituted into (2.23), leads to the parallel stability equations (2.17) for $\omega = 0$. The solution to these equations is obtained using Chebyshev collocation with Gaussian elimination to solve the resulting linear system of equations.

As discussed in detail by Choudhari (1994), the solution of the linear stability equations in Fourier space can be obtained without regard for causality. However, when the Fourier inversion,

$$\boldsymbol{U}'(S,n,z) = \frac{1}{(2\pi)^{1/2}} \int_{\Gamma} \hat{\boldsymbol{U}}(k_s,n) \mathrm{e}^{\mathrm{i}k_s S + \mathrm{i}k_z z} \mathrm{d}k_s, \tag{2.24}$$

is performed to return the solution to physical space, causality must be accounted for in choosing the inversion contour, $\Gamma$. Herein, we assume that the crossflow instability is convective in nature without applying a rigorous causality condition (Bers 1983, Chap. 3.2). This assumption has been used by several researchers in the context of FRNT (Choudhari 1994; Crouch 1994). With this assumption, the contribution of the integral in (2.24) to a particular crossflow instability mode is given by the residue of the integrand at the complex streamwise wavenumber, $\alpha_{cf}$, of the crossflow mode

$$U'(S,n) = \frac{\mathrm{i}(2\pi)^{1/2} \mathrm{e}^{\mathrm{i}\alpha_{cf} S}}{(\partial \hat{U}^{-1}/\partial k_s)(\alpha_{cf},n)}, \tag{2.25}$$

where $\hat{U}$ is an any component of $\hat{\boldsymbol{U}}$. The value of $\partial \hat{U}^{-1}/\partial k_s$ is determined by computing $\hat{U}^{-1}$ at $k_s = \alpha_{cf} \pm \Delta k_s$ and using a second-order-accurate central difference to approximate the derivative.

The form of the complete perturbation vector corresponding to the individual component residues (2.25) for $(s_w, k_z)$ is then given by (Goldstein 1985)

$$\boldsymbol{U}'_{cf}(s,n,z) = \hat{h}_w(\alpha_{cf})\, \Lambda(k_z,s_w)\, \hat{\boldsymbol{U}}_0(n,k_z)\, \mathrm{e}^{\mathrm{i}\alpha_{cf}(s-s_w)+\mathrm{i}k_z z}, \tag{2.26}$$

where $\hat{h}_w(\alpha_{cf})$ is the amplitude of the Fourier component of the roughness shape-function (2.9) which is resonant with the crossflow instability wave with streamwise wavenumber $\alpha_{cf}$, as predicted by linear stability theory applied at $s_w$ with spanwise wavenumber $k_z$. The factor $\Lambda(k_z,s_w)$ is called the 'efficiency' function which characterizes the local receptivity process independent of the geometry of the roughness and $\hat{\boldsymbol{U}}_0(n,k_z)$ is the quasi-parallel eigenfunction for the stationary crossflow mode under consideration.

The efficiency function is determined by equating any component of (2.26) with the appropriate residue given by (2.25). Since the residue depends on both the roughness location and the particular crossflow mode, so too does the efficiency function. However, the particular value of $\Lambda$ depends on the normalization of $\hat{\boldsymbol{U}}_0$. Similar to the stability theory presented in § 2.4, we base all receptivity results on the square-root of the integrated disturbance kinetic energy (2.21) so that the results are independent of the wall-normal coordinate. Thus,

$$\Lambda_{\hat{K}} = |\Lambda| \hat{K}_0, \tag{2.27}$$

where $\hat{K}$ is defined in (2.21). The predicted amplitude of the crossflow instability wave at $s_w$ measured using $\hat{K}$ is then given by

$$A_w = |\hat{h}_w(\alpha_{cf})|\, \Lambda_{\hat{K}}. \tag{2.28}$$

Our implementation of FRNT has been validated against the results of Choudhari (1994) for a Falkner–Skan–Cooke velocity profile and additional details regarding the method and validation are available in Collis (1997).

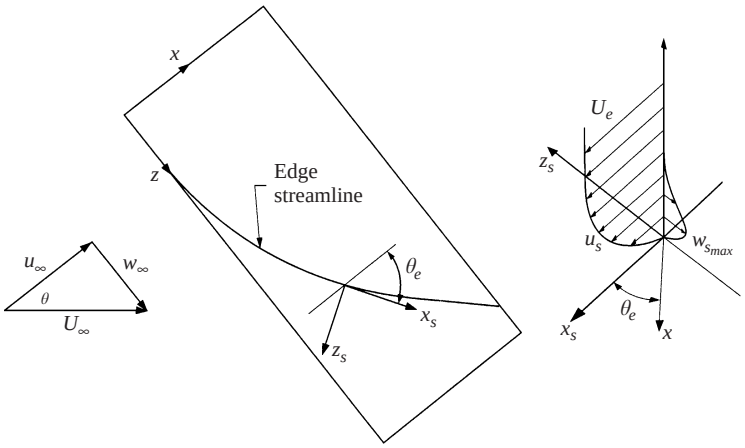


FIGURE 4. Schematic of a three-dimensional boundary layer near a swept leading edge. Surface curvature is not explicitly shown in order to simplify the presentation.

## 3. Results

Results are presented first for the base flow about the parabolic cylinder. Then, the linear stability characteristics of the base flow are determined followed by detailed receptivity results for surface roughness placed near the leading edge.

### 3.1. *Base-flow characteristics*

We begin by documenting the three-dimensional boundary layer over the swept parabolic-cylinder for the conditions: $M = 0.8$, $Re = 1 \times 10^5$, and $\theta = 35°$. Figure 4 shows a schematic of a three-dimensional boundary layer near a swept leading edge which aids in the definition of the various boundary-layer parameters. In this study, the boundary-layer edge is defined as the point where the spanwise, $w$, component of velocity reaches 99.9% of its free-stream value, and quantities at the edge are denoted by a subscript $e$. Since the wing has infinite span, the $w$-velocity profile increases monotonically from zero at the wall to its free-stream value, $\tan(\theta)$. This is in contrast to the more traditionally used $v_s$ velocity. Recall that $v_s$ is the velocity locally tangent to the body at a given station while $v_n$ is the body-normal velocity. These velocity components are related to the global Cartesian velocity components by

$$v_s = n_y u - n_x v, \tag{3.1}$$

$$v_n = n_x u + n_y v, \tag{3.2}$$

where the outward unit-normal to the body is $\boldsymbol{n} = \{n_x, n_y, 0\}^{\mathrm{T}}$. Since the flow is accelerated in the chordwise direction, the $v_s$ velocity outside the boundary layer is greater than the free-stream velocity making an unambiguous definition of the boundary-layer edge difficult. Although the particular choice of edge conditions does have an influence on the reported boundary-layer parameters, the effects are minor and the current approach yields adequate results. Throughout the following discussion, the reader may wish to consult table 1 which itemizes the boundary-layer edge conditions and parameters for selected stations near the leading edge.

The magnitude of the edge velocity, projected to the plane tangent to the body, is given by $U_e = (v_{s_e}^2 + w_e^2)^{1/2}$. In practice, $U_e$ is referred to as the total edge velocity since $v_n$ is negligible except in the immediate vicinity of the attachment line. The edge velocity makes an angle $\theta_e$ with respect to the $x$-axis and this angle is called

| $s$ | $\delta_1$ $\times 100$ | $\delta_2$ $\times 100$ | $U_e$ | $T_e$ | $\theta_e$ (deg.) | $\frac{w_{s_{max}}}{U_e}$ | $\chi$ | $M_e$ | $\beta_h$ |
|---|---|---|---|---|---|---|---|---|---|
| 0.000 | 0.324 | 0.119 | 0.700 | 1.128 | 90.0 | 0.000 | 0 | 0.527 | 1.000 |
| 0.020 | 0.324 | 0.119 | 0.700 | 1.128 | 88.7 | −0.006 | 7 | 0.527 | 1.000 |
| 0.041 | 0.324 | 0.119 | 0.700 | 1.128 | 87.3 | −0.012 | 14 | 0.527 | 0.999 |
| 0.085 | 0.324 | 0.120 | 0.703 | 1.128 | 84.5 | −0.024 | 28 | 0.529 | 0.996 |
| 0.109 | 0.325 | 0.120 | 0.705 | 1.127 | 82.9 | −0.031 | 36 | 0.531 | 0.993 |
| 0.136 | 0.325 | 0.120 | 0.708 | 1.127 | 81.2 | −0.038 | 45 | 0.533 | 0.989 |
| 0.197 | 0.326 | 0.121 | 0.717 | 1.125 | 77.5 | −0.053 | 63 | 0.540 | 0.978 |
| 0.233 | 0.328 | 0.122 | 0.723 | 1.124 | 75.4 | −0.061 | 73 | 0.545 | 0.970 |
| 0.273 | 0.329 | 0.123 | 0.731 | 1.122 | 73.2 | −0.069 | 84 | 0.552 | 0.960 |
| 0.368 | 0.334 | 0.125 | 0.752 | 1.118 | 68.5 | −0.084 | 105 | 0.569 | 0.931 |
| 0.423 | 0.338 | 0.127 | 0.766 | 1.116 | 66.0 | −0.090 | 116 | 0.580 | 0.912 |
| 0.485 | 0.344 | 0.129 | 0.781 | 1.113 | 63.6 | −0.096 | 126 | 0.592 | 0.890 |
| 0.553 | 0.351 | 0.132 | 0.799 | 1.109 | 61.1 | −0.101 | 136 | 0.607 | 0.864 |
| 0.712 | 0.371 | 0.140 | 0.838 | 1.101 | 56.5 | −0.106 | 153 | 0.639 | 0.801 |
| 0.802 | 0.384 | 0.144 | 0.860 | 1.096 | 54.5 | −0.107 | 161 | 0.657 | 0.765 |
| 0.904 | 0.400 | 0.150 | 0.881 | 1.091 | 52.5 | −0.106 | 168 | 0.675 | 0.727 |
| 1.014 | 0.419 | 0.156 | 0.903 | 1.086 | 50.8 | −0.105 | 174 | 0.693 | 0.688 |
| 2.091 | 0.618 | 0.221 | 1.030 | 1.055 | 42.8 | −0.087 | 208 | 0.803 | 0.425 |
| 4.098 | 0.953 | 0.326 | 1.111 | 1.033 | 39.0 | −0.066 | 232 | 0.874 | 0.241 |
| 6.167 | 1.239 | 0.415 | 1.143 | 1.024 | 37.7 | −0.055 | 242 | 0.904 | 0.168 |
| 8.210 | 1.483 | 0.491 | 1.159 | 1.019 | 37.1 | −0.048 | 248 | 0.919 | 0.131 |
| 10.013 | 1.676 | 0.550 | 1.169 | 1.016 | 36.8 | −0.043 | 251 | 0.928 | 0.110 |
| 15.479 | 2.175 | 0.705 | 1.185 | 1.011 | 36.2 | −0.034 | 255 | 0.943 | 0.075 |
| 20.261 | 2.544 | 0.818 | 1.192 | 1.009 | 35.9 | −0.030 | 256 | 0.949 | 0.060 |
| 25.164 | 2.879 | 0.922 | 1.197 | 1.007 | 35.8 | −0.027 | 255 | 0.954 | 0.049 |
| 30.121 | 3.185 | 1.016 | 1.200 | 1.006 | 35.7 | −0.024 | 254 | 0.957 | 0.042 |
| 40.092 | 3.733 | 1.186 | 1.204 | 1.005 | 35.5 | −0.021 | 251 | 0.961 | 0.033 |
| 50.083 | 4.216 | 1.335 | 1.207 | 1.004 | 35.4 | −0.018 | 249 | 0.964 | 0.027 |

TABLE 1. Swept parabolic-cylinder boundary-layer characteristics for $M = 0.8$, $Re = 1 \times 10^5$, $\theta = 35^\circ$, $Pr = 1$, and $T(s, 0, z) = T_0$. Crossflow Reynolds number, $\chi$, is defined in (3.5) and the Hartree parameter, $\beta_h$, is defined by (3.6).

the local sweep angle. When presenting boundary-layer profiles, it is useful to convert the velocity to a coordinate system that is locally aligned with the edge velocity. Velocity components in this 'streamline' coordinate system are denoted by $(u_s, v_n, w_s)$, where $u_s$ is the local, streamwise velocity, $v_n$ is the body-normal velocity, and $w_s$ is the crossflow velocity. These components are related to the velocities in the boundary-fitted coordinate system by

$$u_s = \cos(\theta_e) v_s + \sin(\theta_e) w, \tag{3.3}$$

$$w_s = -\sin(\theta_e) v_s + \cos(\theta_e) w. \tag{3.4}$$

With these definitions, we begin to examine the characteristics of this three-dimensional boundary-layer. Figure 5 shows streamwise, $u_s$, and crossflow, $w_s$, velocity profiles at three stations near the leading edge where the profiles have been non-dimensionalized by $U_e$. The streamwise profile is Blasius-like while the crossflow profile is inflectional giving rise to the inviscid, crossflow instability.

For this flow, the standard attachment-line length scale $\delta_l^* \equiv [v_e^*/(\partial U_e^*/\partial s^*)]^{1/2}$ is $0.00304\, r_n^*$ and this yields an attachment-line Reynolds number $\bar{R} \equiv \delta_l^* w_\infty^*/v_\infty^*$ of 213.

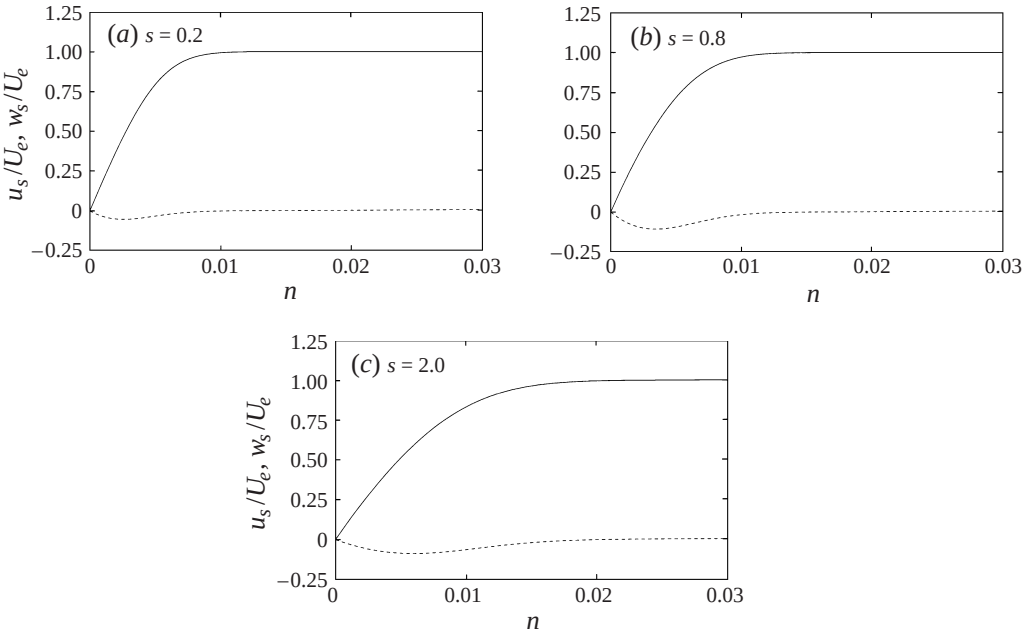


FIGURE 5. Velocity profiles in local streamwise coordinates: ——, $u_s/U_e$; - - - -, $w_s/U_e$.

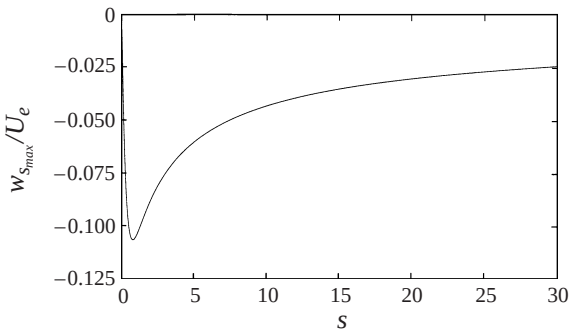


FIGURE 6. Maximum, in $n$, of the crossflow component of velocity normalized by the local edge velocity.

This value of $\bar{R}$ is less than the critical value of 583, which ensures that the flow is linearly stable along the attachment line (Spalart 1989).

Figure 6 shows the chordwise evolution of the maximum crossflow component of velocity normalized by the local edge velocity. The normalized crossflow component is everywhere negative and reaches its greatest magnitude of $-0.107$ at $s = 0.802$. At the point of maximum normalized crossflow, the crossflow Reynolds number

$$\chi \equiv \delta^*_{0.999} w^*_{s\,max}/\nu^*_e \tag{3.5}$$

is 161. The results of Poll (1985) for a swept circular cylinder indicate that the critical crossflow Reynolds number is 125 and our value of 161 suggests that significant crossflow instability will be present. Table 1 shows that the crossflow Reynolds number reaches a maximum of 256 at $s \approx 20.3$.

The variation of the local sweep angle, $\theta_e$, of the edge velocity is shown in figure 7.

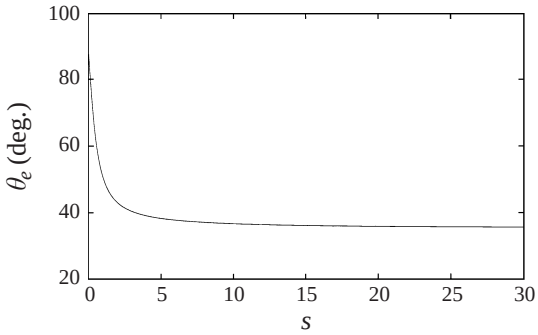


FIGURE 7. Evolution of the local sweep angle, $\theta_e$.

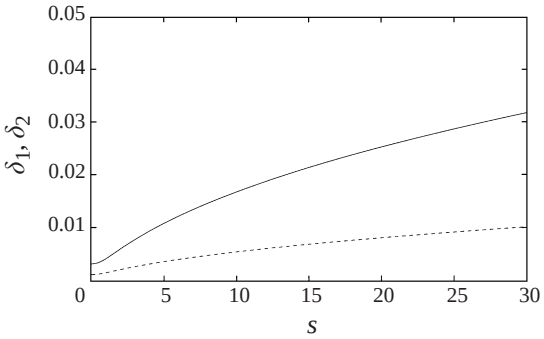


FIGURE 8. ——, Boundary layer displacement thickness, $\delta_1$, and - - - -, momentum thickness, $\delta_2$.

At the point of maximum normalized crossflow velocity, the local sweep angle is 54.5° relative to the chord compared to a value of 90° at the attachment line. Downstream, the local sweep angle asymptotes to the global sweep angle $\theta = 35°$ as the chordwise pressure gradient decays. The pressure gradient along the parabola is documented using the Hartree pressure-gradient parameter which is defined as

$$\beta_h = \frac{2m}{m+1}, \qquad \text{where} \qquad m = \frac{s}{u_s}\frac{\partial u_s}{\partial s}. \tag{3.6}$$

Table 1 lists values of $\beta_h$ along the length of the plate. At the attachment line, $\beta_h = 1$, corresponding to an impingement flow in the $(x, y)$-plane, while downstream of the leading edge, $\beta_h$ decays monotonically to zero. At the point of maximum normalized crossflow, $\beta_h = 0.765$ and by 30 nose radii downstream $\beta_h$ is reduced to 0.042 indicating that the flow is approaching a zero-pressure-gradient boundary layer.

Figure 8 shows the displacement and momentum thickness evolution for the local streamwise velocity profile. The streamwise displacement thickness is defined by

$$\delta_1 \equiv \int_0^{\delta_{0.999}} \left(1 - \frac{\rho u_s}{\rho_e U_e}\right) \mathrm{d}n \tag{3.7}$$

while the streamwise momentum thickness is given by

$$\delta_2 \equiv \int_0^{\delta_{0.999}} \frac{\rho u_s}{\rho_e U_e}\left(1 - \frac{u_s}{U_e}\right) \mathrm{d}n. \tag{3.8}$$

As validation of our numerical method, we compare the attachment-line thickness

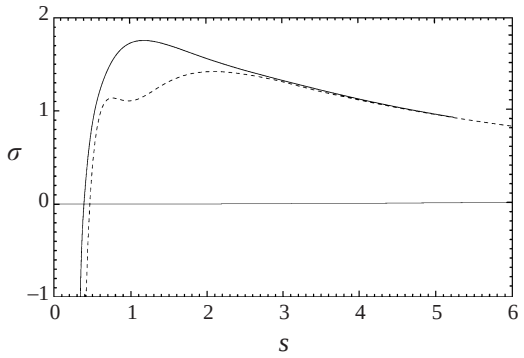


FIGURE 9. Spatial growth rate for $k_z = 35$: ——, LNS and - - - -, non-parallel linear stability theory (LST) with curvature.

ratio, $\delta_2/\delta_l$, from the current solution to that of the compressible similarity solution (Reshotko & Beckwith 1958; Topham 1965). From the data in table 1, $\delta_2/\delta_l = 0.3926$ while the similarity solution under the same conditions gives 0.4020. As pointed out by a referee, this 2.3% difference is primarily due to our use of a constant viscosity while the similarity solution is based on a linear viscosity–temperature relation. To verify this, we have repeated our mean-flow calculation using a linear viscosity relation with the result $\delta_2/\delta_l = 0.3989$ that is within 0.8% of the similarity solution. This excellent agreement provides additional validation of our numerical method.

### 3.2. *Linear stability characteristics*

The stability and receptivity characteristics of the three-dimensional boundary layer on the swept parabolic cylinder are studied for two spanwise wavenumbers $k_z = 35$ and $k_z = 100$. The $k_z = 35$ wavenumber corresponds to a relatively long-wavelength stationary crossflow instability mode which is very nearly the most dangerous mode (i.e. the mode which has the greatest amount of linear growth). The $k_z = 100$ mode is a relatively short-wavelength crossflow mode for which non-parallel effects are expected to be significantly reduced as compared to the $k_z = 35$ mode.

The stability characteristics of the three-dimensional boundary layer for $k_z = 35$ are shown in figure 9. This figure shows the spatial growth rate, $\sigma$ (based on the integrated disturbance kinetic energy) obtained using two different techniques. The solid line shows the results from a LNS calculation where the crossflow eigenfunction was forced on the inflow boundary of the computational domain, upstream of the first neutral point. The numerical method used to obtain this solution is identical to that outlined in § 2.3 except that the linear stability eigenfunction is forced on the inflow boundary and the wall is smooth (see Chapter 5 of Collis 1997). The dashed line corresponds to the growth rate predicted by the linear stability analysis of § 2.4 which includes an exact account of surface curvature and a perturbation technique for non-parallel effects. For $s > 3$ the agreement between the computed solution and stability theory is excellent. However, for $s < 3$ there is clearly a significant deviation, indicating that the perturbation approach used in the non-parallel theory is inadequate in this region. A detailed discussion of the failure of non-parallel stability theory is given in Collis (1997).

Similar spatial growth-rate results are shown for $k_z = 100$ in figure 10. For this shorter wavelength, the non-parallel stability theory is in excellent agreement with the computed solution over the entire unstable region. For this relatively short spanwise

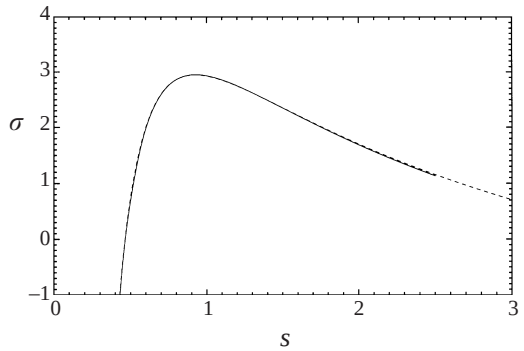


FIGURE 10. Spatial growth rate for $k_z = 100$: ——, LNS and - - - -, non-parallel LST with curvature.

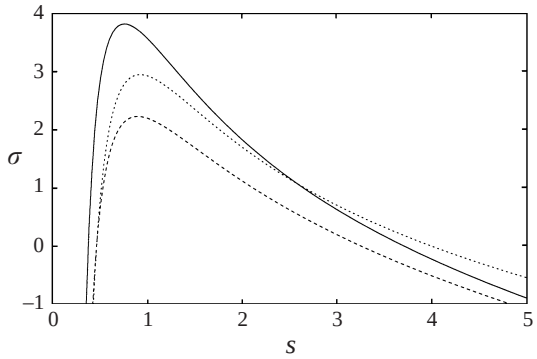


FIGURE 11. Comparison of crossflow growth-rate predictions for $k_z = 100$: ——, parallel LST; - - - -, parallel LST with curvature; · · · · ·, non-parallel LST with curvature.

wavelength, the non-parallel effects near the leading edge are significantly reduced and the perturbation approach in the linear stability analysis is adequate.

The linear stability results obtained for the parabolic cylinder are qualitatively similar to previous results for the circular cylinder (Masad & Malik 1994). This is demonstrated in figure 11 where linear stability growth-rate predictions for $k_z = 100$ are shown. When convex surface curvature is included in the analysis, the growth rate is dramatically reduced over the entire unstable range of $s$ compared to parallel, flat-plate theory. The addition of the non-parallel correction leads to an increase in the predicted growth rate although, near the peak growth rate, the increase due to non-parallelism is less than the decrease due to curvature making the actual growth rate less than the quasi-parallel, flat-plate prediction for this mode. As shown above, the combined theory with curvature and non-parallel effects is in excellent agreement with LNS for this wavenumber. These results lead to the conclusion that convex surface curvature generally causes a reduction in the growth rate of stationary crossflow instability waves while non-parallel effects increase the growth rate and this is consistent with the findings of Masad & Malik (1994) for the swept circular cylinder. Similar results are obtained for the $k_z = 35$ mode; however, as shown above, the perturbation approximation for non-parallel effects is unable to accurately predict the growth rate of the $k_z = 35$ mode near the leading edge and the full LNS equations are required to determine the stability characteristics.

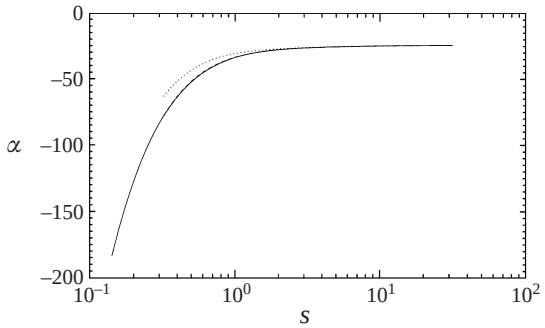


FIGURE 12. Comparison of crossflow wavenumber predictions for $k_z = 35$: ——, parallel LST; - - - -, parallel LST with curvature; · · · · ·, non-parallel LST with curvature.

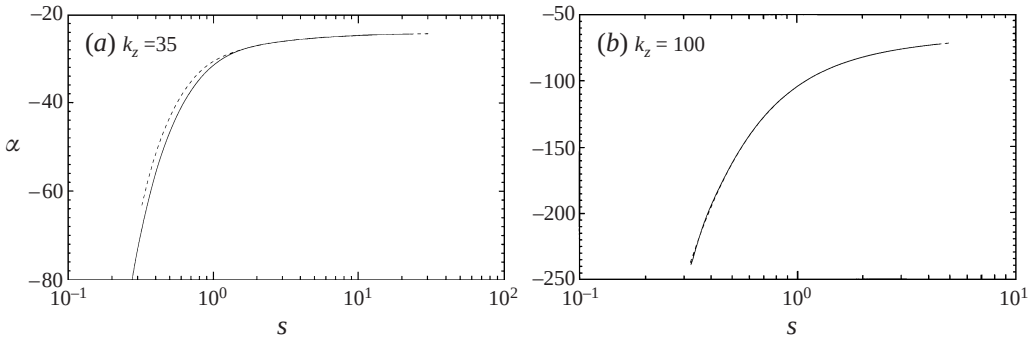


FIGURE 13. Crossflow instability wavenumber: ——, LNS; - - - -, is non-parallel LST with curvature.

The chordwise wavenumber from LST for $k_z = 35$ is shown in figure 12 where a log scale is used in $s$ to highlight the leading-edge behaviour. Curvature is seen to have little influence on the wavenumber while non-parallel effects tend to decrease the wavenumber magnitude. This decrease is most pronounced near the leading edge but it also occurs, to a lesser degree, over the entire unstable range. Figure 13 shows the crossflow wavenumber extracted from LNS solutions compared to LST with curvature and non-parallel corrections. Similar to the growth-rate results, the wavenumber from the non-parallel theory is in good agreement with LNS for $k_z = 100$, but for $k_z = 35$ the wavenumber predicted by theory is inaccurate upstream of $s = 1$.

Figure 14 shows the $N$-factor where

$$N = \int_{s_I}^{s} \sigma(s)\, \mathrm{d}s \tag{3.9}$$

and $s_I$ is the location where the mode first becomes unstable. To compute the $N$-factor, the growth rate extracted from the LNS solution is utilized since the stability theory is inaccurate for $k_z = 35$. ($N$-factor comparisons based on LNS and stability theory are given in Collis (1997).) The $N$-factor is commonly used in wing design to predict the location of the laminar-to-turbulent transition. In practice, a value of $N \approx 10$ is often taken as the transition location although, in reality, $N$ at transition is a function of the disturbance environment and instability mechanism(s) (Malik 1990). From the figure, we see that the $k_z = 35$ mode reaches a considerably larger value of $N$ compared to the $k_z = 100$ mode. In fact, for these flow conditions, $k_z = 35$

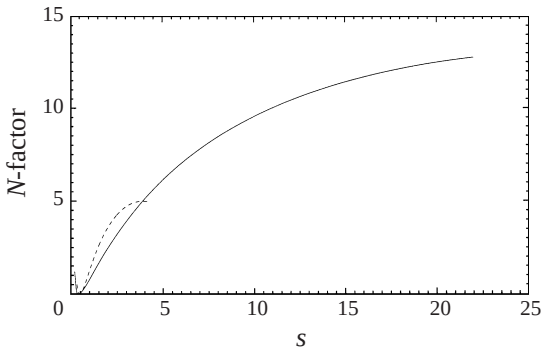


FIGURE 14. Evolution of the $N$-factor for ——, $k_z = 35$ and - - - -, $k_z = 100$.

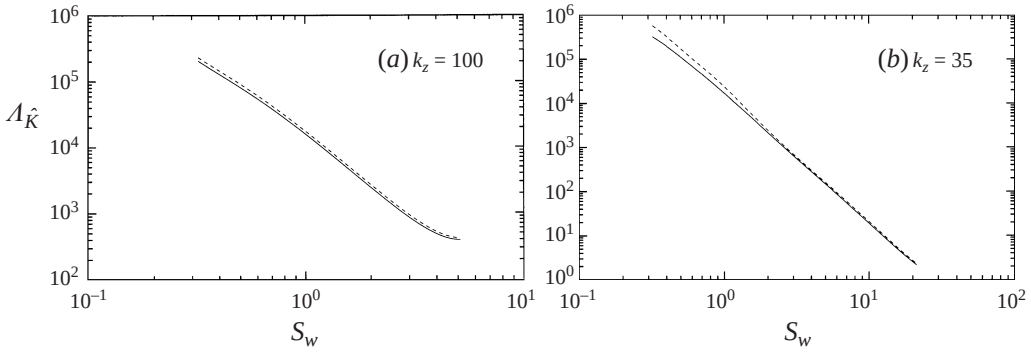


FIGURE 15. FRNT receptivity efficiency function: ——, no curvature and - - - -, with curvature.

is approximately the most dangerous crossflow mode which is the motivation for studying the stability and receptivity characteristics of this mode. Given that $k_z = 35$ is the most dangerous mode, it is particularly unfortunate that the non-parallel perturbation approach fails to accurately predict its stability characteristics and the implication of this for receptivity predictions is discussed below.

### 3.3. *Receptivity predictions*

We begin our investigation of receptivity by applying FRNT, discussed in § 2.5, to the mean boundary-layer profiles on the parabolic cylinder. Figure 15 shows the receptivity efficiency factor, $\Lambda_{\hat{K}}$, for $k_z = 100$ and $k_z = 35$ as a function of roughness location. Recall that $\Lambda_{\hat{K}}$ is proportional to the initial amplitude of an instability wave but is independent of the geometry of the roughness. An interesting, and previously undocumented, result that follows from figure 15 is that convex curvature increases the efficiency of the receptivity process for this flow. This result holds true over the full range of unstable spanwise wavenumbers as seen in figure 16 which shows the variation of $\Lambda_{\hat{K}}$ with $k_z$ for roughness located near the maximum normalized crossflow velocity, $s_w = 0.8$, both with and without curvature. The increase in receptivity efficiency due to curvature is most pronounced near the first neutral point ($k_z \approx 40$) where there is a local maximum in the receptivity efficiency. A similar local maxima has been observed by Crouch (1993) for an incompressible Falkner–Skan–Cooke boundary layer on a flat plate. With the exception of the region immediately surrounding the lower neutral point, curvature causes a relatively uniform increase of

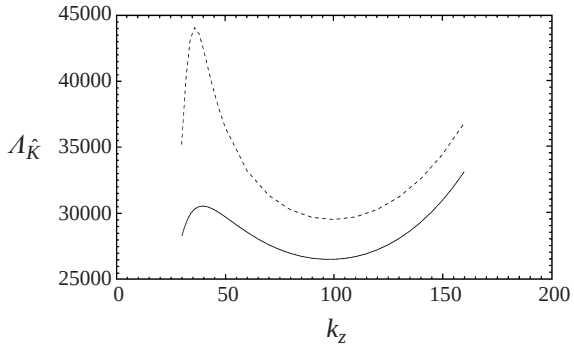


FIGURE 16. Variation of the receptivity efficiency with spanwise wavenumber for $s_w = 0.8$: ——, no curvature and - - - -, with curvature.

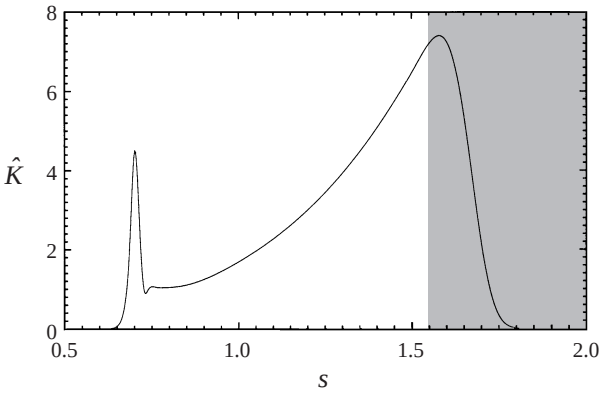


FIGURE 17. Evolution of $\hat{K}$ for $k_z = 100$, $s_w = 0.7$, and $\sigma_w = 0.01$. Shaded region is the outflow sponge.

10% in the receptivity efficiency factor at this station. When interpreting the results in figure 15, it is important to realize that $\Lambda_{\hat{K}}$ is the response for a Dirac delta function bump in $s$ (i.e. it is the Green's function response). This explains why $|\Lambda|$ increases without bound as $s_w$ is decreased since the delta function has a unit spectrum for all $k_s$. The actual amplitude, as given by (2.28), is modulated by the Fourier spectrum in $s$ of the bump shape, $h_w$, which limits the amplitude for a fixed bump width as $s_w$ is decreased. The increase in receptivity efficiency due to convex curvature is particularly interesting given the fact that convex curvature has a stabilizing effect on the growth of crossflow modes as shown in § 2.4. The reduced growth rate with convex curvature is offset, to some degree, by a greater initial amplitude. Of course, the net impact of curvature depends on the particular conditions.

To evaluate the accuracy of FRNT predictions and to determined the impact of non-parallel effects, LNS solutions have been computed for a variety of roughness locations and the effective amplitude of the dominant stationary crossflow instability wave at the roughness location has been extracted from each solution. Typical results are shown in figure 17 which plots the evolution of $\hat{K}$ for a bump with $k_z = 100$ located at $s_w = 0.7$ with $\sigma_w = 0.01$. Near the roughness site, $\hat{K}$ has roughly the shape of the imposed Gaussian bump. Downstream, there is a mild transient as the spatially damped modes excited by the bump quickly decay. By $s = 1.2$, the response

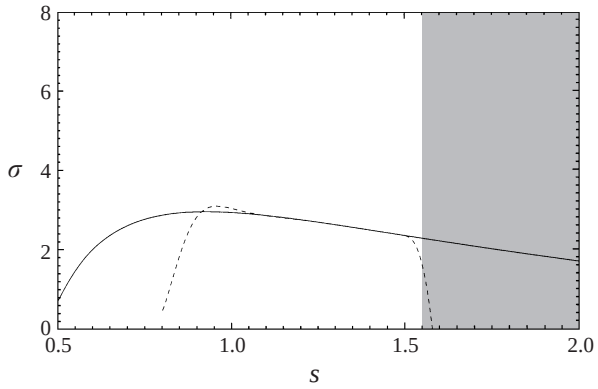


FIGURE 18. Growth rate based on $\hat{K}$ for $k_z = 100$: - - - -, extracted from receptivity solution with $s_w = 0.7$ and $\sigma_w = 0.01$; ——, LNS stability solution. Shaded region is the outflow sponge for the receptivity calculation.

is dominated by the unstable crossflow mode and this continues to $s = 1.5$ where the outflow sponge begins to damp the crossflow mode. From the variation of $\hat{K}$ with $s$, the spatial growth rate is determined using

$$\sigma = \mathrm{Re}\left[\frac{\partial}{\partial s}\ln(\hat{K})\right], \tag{3.10}$$

and the computed growth rate is shown in figure 18 compared to the LNS stability solution taken from figure 10. Downstream of $s = 1.2$ and until slightly upstream of the sponge, the two growth rates are in excellent agreement. Upstream of $s = 1.2$, the transient flow due to decaying modes excited by the bump leads to large oscillations in the spatial growth rate (only a portion of the oscillation is shown). As a general procedure for extracting the amplitude of the dominant crossflow mode, we compare the growth rate from the receptivity calculation with the stability theory results of § 3.2. Since the growth rate is a very sensitive indication of transient behaviour, this comparison allows the determination of a location, $s_l$, where the transient is negligible. For the case shown here, we selected $s_l = 1.4$ and measured the amplitude of the response at this location, $A_l$, based on $\hat{K}(s_l)$.

To compare the LNS receptivity results to FRNT requires that the crossflow instability amplitude be extrapolated from $s_l$ back to $s_w$, since the theory predicts the amplitude at this location. For this purpose, we use the $N$-factor shown in figure 14. The amplitude at $s_w$ is then given by

$$A_w = A_l \mathrm{e}^{(N(s_w)-N(s_l))}. \tag{3.11}$$

Note that since the $N$-factor in figure 14 is computed from a LNS stability calculation, it takes exact account of curvature and non-parallel effects. Thus, there is no approximation in the extrapolation.

Using this technique, figure 19 shows the extracted crossflow instability amplitude for $k_z = 100$ and $k_z = 35$. For $k_z = 35$ a roughness width of $\sigma_w = 0.05$ is used while a narrower roughness distribution $\sigma_w = 0.01$ is utilized for the higher spanwise wavenumber, $k_z = 100$. These particular roughness widths were selected to provide reasonable initial crossflow amplitudes at the first neutral point without requiring excessive resolution near the roughness location. Since the roughness width is fixed, the amplitude of the resulting crossflow mode eventually drops as the bump is moved

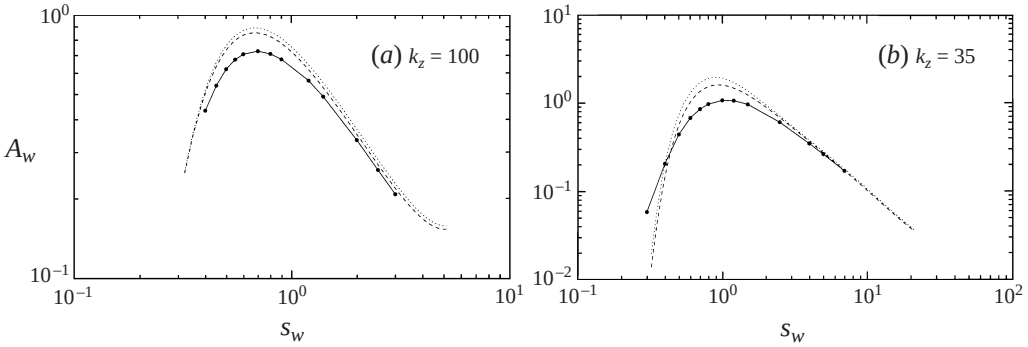


FIGURE 19. Effective amplitude at the bump location for $k_z = 35$, $\sigma_w = 0.05$ and $k_z = 100$, $\sigma_w = 0.01$: —●—, LNS solution; - - - -, FRNT no curvature; · · · · ·, FRNT with curvature.

towards the leading edge, since the magnitude of the streamwise wavenumber of the crossflow mode increases (see figure 13) thus reducing the effective forcing amplitude of the roughness due to a reduction in the magnitude of the Fourier transform of the Gaussian roughness distribution (2.9). In addition to the LNS receptivity results, figure 19 also shows FRNT receptivity predictions for the crossflow amplitude using (2.28) in § 2.5.

First consider the results for $k_z = 100$ shown in figure 19(*a*). The amplitude, $A_w$, generally follows the same trend as the efficiency factor for large $s_w$, with $A_w$ increasing as $s_w$ is reduced. At about $s_w = 0.65$, there is a maximum in $A_w$ which is associated with the Fourier spectrum of the roughness distribution with $\sigma_w = 0.01$. When comparing the LNS results to the FRNT predictions, the first observation is that FRNT over-predicts the amplitude, by as much as 29% with curvature and 21% without curvature. Based on these results, it is obvious that non-parallel effects tend to reduce the amplitude of crossflow vortices generated by roughness. Similar to curvature, this result is opposite to that observed for stability characteristics, where non-parallel flow, generally speaking, destabilizes crossflow vortices (see § 3.2). Downstream of the maximum, the FRNT predictions approach the LNS solution, as expected, with the no-curvature prediction in slightly better agreement than the prediction with curvature. The fact that the FRNT prediction without curvature is in better agreement with the LNS solution is similar to the stability results where the growth rate with curvature is a worse approximation to the actual growth rate than the local flat-plate prediction. Since non-parallel and curvature effects are competing, including only one of the effects can result in a prediction which is in greater error than the original parallel, flat-plate value.

Amplitude results for $k_z = 35$ are shown in figure 19(*b*). Similar to the $k_z = 100$ case, both FRNT results significantly over-predict the crossflow amplitude near $s_w = 1$. The greater non-parallel effects for this long spanwise wavelength are evident in the maximum error which is 77% with curvature and 45% without. For roughness locations beyond approximately $s_w = 5$, the FRNT amplitudes are in reasonably good agreement with LNS. However, upstream of the neutral point at $s_w = 0.40$, the FRNT amplitudes are slightly lower than the LNS values. This crossover in FRNT and LNS solutions (which is also likely to occur for $k_z = 100$ for small $s_w$) is due to the error in the parallel-flow LST wavenumber used to evaluate $\hat{h}(\alpha_{cf})$ in the FRNT.

The receptivity results presented so far have been for fixed roughness width. For moderately sized bumps, the actual value of $\sigma_w$ is not expected to alter the qualitative

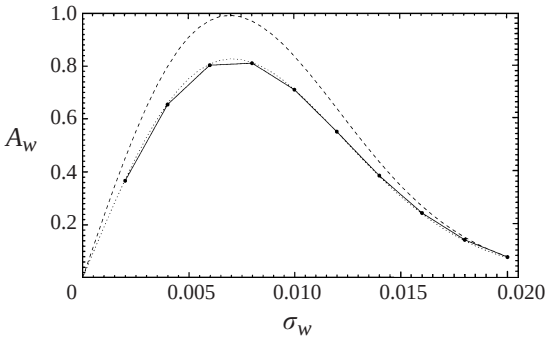


FIGURE 20. Variation of $A_w$ with $\sigma_w$ at $s_w = 0.6$, $k_z = 100$. —●—, LNS; - - - -, FRNT no curvature; · · · · ·, curve fitted to the LNS results using $|\Lambda| = 193$, $\alpha_{cf} = -142$.

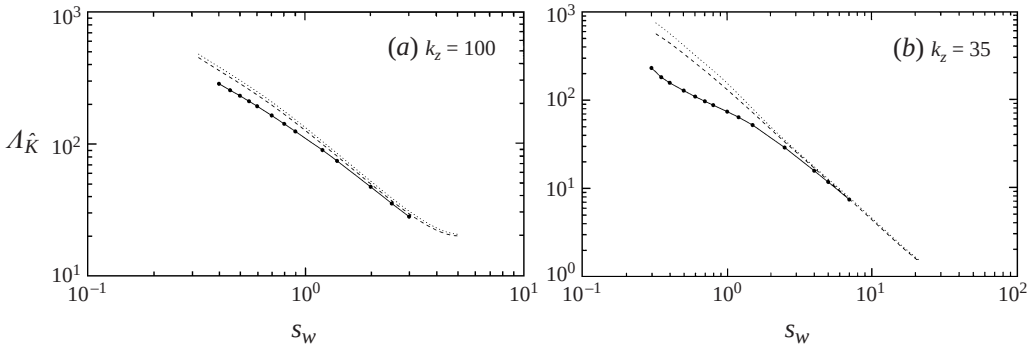


FIGURE 21. Receptivity efficiency function for $k_z = 35$ and $k_z = 100$: —●—, computed; - - - -, FRNT no curvature; · · · · ·, FRNT with curvature.

comparison to FRNT. This is demonstrated in figure 20 which shows the effect of $\sigma_w$ on the initial crossflow amplitude with the bump placed at $s_w = 0.6$ and $k_z = 100$. As expected, the FRNT prediction overestimates the amplitude for all $\sigma_w$. However, the functional dependence of $A_w$ on $\sigma_w$ is correctly predicted by FRNT. This is demonstrated by setting $\alpha_{cf} = -142$, which is the value based on $|\hat{v_s}|_{max}$ from the LNS stability calculation (see figure 13), and adjusting $\Lambda_{\hat{K}}$ in (2.28) to generate a curve that fits the LNS data. Excellent agreement is achieved for $\Lambda_{\hat{K}} = 193$ and this curve is also shown in figure 20. We point out that estimating $\Lambda_{\hat{K}}$ in this manner is only an approximation, since the value of $\alpha_{cf}$ used to evaluate $|\hat{h}_w|$ is not necessarily the 'correct' value. In fact, here we use only the real component of the wavenumber in estimating $\Lambda_{\hat{K}}$ since the imaginary component is at least two orders of magnitude smaller. A better fit could be obtained by optimizing both $\alpha_{cf}$ and $\Lambda_{\hat{K}}$, but the improvement is only slight.

Given the success of the current method, we have used the same procedure to estimate the value of $\Lambda_{\hat{K}}$ from the LNS solutions at other chordwise stations. Using $\alpha_{cf}$, based on $|\hat{v_s}|_{max}$ from the LNS stability calculation, (2.9) is used to compute the local value of $|\hat{h}_w|$ and (2.28) is then solved for $\Lambda_{\hat{K}}$. The results, for both values of $k_z$, are shown in figure 21 along with the FRNT predictions from figure 15. For both spanwise wavenumbers, the receptivity efficiencies from LNS and FRNT approach one another for large $s_w$ ($\approx 5\%$ difference at the furthest downstream station). This is consistent with the reduction in non-parallel effects with increasing $s_w$ observed in the

stability analysis. Near the leading edge (i.e. roughness locations upstream of $s_w = 1$), non-parallel effects increase causing FRNT to over-predict the receptivity efficiency. The influence of non-parallel effects is more pronounced for the $k_z = 35$ mode, which is also consistent with the linear stability results. For roughness placed at the upstream neutral point, $s_w = 0.395$ for $k_z = 35$, the FRNT result with curvature has an error of 264% while the prediction without curvature has a 182% error. For $k_z = 100$ the errors in the FRNT are reduced considerably to 32.2% for FRNT with curvature, and 24.5% without curvature. For both spanwise wavenumbers, non-parallel effects decrease the receptivity efficiency over the entire unstable region, but the decrease is greatest near the leading edge. We note that since a perturbation approximation to non-parallel effects was unable to predict the stability characteristics for $k_z = 35$ near the leading edge, is is possible that a first-order perturbation scheme used to correct the parallel FRNT receptivity predictions may also fail in this region – especially since FRNT predictions inherently depend on the underlying stability characteristics. Future research is required to investigate non-parallel receptivity predictions.

### 3.4. *Discussion of results*

The results presented in the previous sections have identified curvature and non-parallel effects as having a significant quantitative impact on the initial amplitude of stationary crossflow vortices downstream of a localized roughness element. Given the previously documented (Masad & Malik 1994; Malik & Balakumar 1993) effect of both curvature and non-parallelism on the growth characteristics of crossflow modes, their impact on receptivity is not surprising. What is interesting, however, is that curvature, known to stabilize crossflow vortices, actually enhances receptivity, while non-parallel effects, which typically destabilize crossflow modes, are found to attenuate the initial crossflow amplitude. For the limited range of parameters investigated here, the attenuation due to non-parallel effects is greater than the enhancement due to convex surface curvature. Progressing downstream on the parabolic cylinder, curvature and non-parallel effects are naturally reduced so that the FRNT predictions approach the LNS solution for large values of the roughness location, $s_w$. However, the effect of non-parallelism is still evident at the furthest downstream stations investigated and the amplitudes predicted by FRNT are consistently greater than the LNS solution. The fact that non-parallel effects are so significant for this flow stems from the fact that the first neutral point for crossflow vortices typically lies very close to the leading edge. Choudhari (1994), when presenting FRNT results for FSC profiles, cautions that since the neutral point for crossflow vortices occurs near the leading edge for realistic geometries, non-parallel effects may be important. This hypothesis is clearly substantiated by the current results where the error in the predicted amplitude (with curvature) is as high as 77% just downstream of the neutral point.

To put this in perspective, assume that, given the actual initial amplitude of the instability wave, transition occurs with $N = 10$ such that $s_{tr} = 11.0$ based on the stability data in figure 14 for $k_z = 35$. Using FRNT, our estimate of the initial amplitude would be 77% too high which is equivalent to an $N$-factor difference of 1.5. Thus, transition would be incorrectly predicted when $N = 8.5$, corresponding to $s_{tr} = 8.15$, which is an error of 26% in the transition location. In this case, FRNT leads to a transition location prediction which is outside of typically accepted engineering accuracy. In the context of a laminar-flow wing, if we assume that transition occurs at $x/c = 0.7$ then a 26% error in the transition prediction leads to $x/c = 0.52$ for a difference of 18% chord. This is indeed a significant error in the transition location – the additional 18% chord may be the difference between economic viability and

design failure. This is further exacerbated when one includes sources of uncertainty in the transition prediction process, including unknown environmental disturbances, bugs, dust, etc. Each of these inherently unknown factors requires an engineering safety factor. If we start with a fixed error of 18% and add safety factors to account for uncertainties, we are quickly left with a design that is predicted to be impractical, when in fact it may be feasible.

It is interesting to compare the current findings to the recent study by Crouch & Spalart (1995) who investigated the influence of non-parallel effects on the receptivity of a two-dimensional boundary layer with localized suction subjected to a free-stream acoustic wave. Comparing numerical simulations with FRNT predictions, they found that the theory is in very good agreement with simulations downstream of the first neutral point for the prediction of Tollmien–Schlichting wave amplitudes. At the neutral point, the theory under-predicts the amplitude by 4% and this difference increases further upstream to a value between 6.5% and 11.2%. Based on these results, they conclude that neglecting the weak boundary-layer growth in the receptivity theory is an acceptable approximation for this flow. Based on the current results, the conclusion of Crouch & Spalart obviously does not apply for crossflow instability. It is particularly interesting to note that they found non-parallel effects to slightly increase the receptivity amplitude for Tollmien–Schlichting waves, while we find that initial crossflow vortex amplitudes are generally attenuated by non-parallel effects. This is in contrast with the influence of non-parallel flow on stability characteristics. Fasel & Konzelmann (1990), in comparisons of Navier–Stokes solutions and stability analysis, show that for Tollmien–Schlichting waves in a Blasius boundary layer, non-parallel effects lead to an increase in the growth rate. Similarly, we have shown that non-parallel flow also destabilizes crossflow vortices. Thus, there is no apparent trend linking stability and receptivity results concerning non-parallel effects. However, we note that the receptivity and stability processes under consideration are quite different, and this statement must be considered in this light.

## 4. Conclusions

Receptivity to surface roughness has been investigated by modelling a roughness element as a spanwise-periodic, linear perturbation of the wall boundary with a Gaussian distribution in the chordwise direction. Receptivity results are obtained both from Linearized Navier–Stokes (LNS) solutions and from Finite Reynolds Number Theory (FRNT) predictions. The theoretical predictions are determined both with and without surface curvature to identify its effect on receptivity. Based on the theoretical predictions, curvature is shown to enhance the receptivity efficiency over the entire unstable region and the curvature effect is greatest near the lower branch of the neutral curve. The impact of non-parallel flow on the receptivity of crossflow instability waves is established by a series of LNS calculations with surface roughness placed at various locations on the wall. Comparison to the FRNT shows that non-parallel flow significantly attenuates the initial amplitude of stationary crossflow instability waves downstream of a roughness element near the leading edge. The effect is most severe for the long-wavelength $k_z = 35$ case where FRNT over-predicts the amplitude of the crossflow mode by as much as 77%. For the shorter-wavelength case, $k_z = 100$, the maximum error in the FRNT prediction is 29%. Sufficiently far from the leading edge, the theoretical predictions approach the computed solution and are within 5% of the computed solution at the furthest downstream stations considered here.

We have verified the FRNT result that the receptivity amplitude can be written as the product of the Fourier coefficient of the chordwise roughness distribution at the local crossflow wavenumber and a function representing the efficiency of the receptivity process. Based on this form of the solution, the receptivity efficiency function is extracted from the computed solutions. The results indicate conclusively that non-parallel effects dramatically reduce receptivity near the leading edge. For the cases considered here, the FRNT over-predicts the efficiency function by as much as a factor of 3 near the first neutral point. These results clearly indicate that the accurate prediction of crossflow instability receptivity near a realistic leading edge must account for the strongly non-parallel flow near the upstream neutral point. Unfortunately, stability predictions using a perturbation approach for non-parallel effects proved inadequate for the most dangerous crossflow mode for the conditions studied. Thus, perturbation approaches for theoretical non-parallel receptivity prediction may also prove inadequate; however further research is required to verify this claim.

This research was supported in part by a NSF fellowship to S.S.C. and by a NSF-PYI award (grant number CTS-9158142-004) to S.K.L. with industrial matching support from the Boeing Company. Computer time was provided by the San Diego Supercomputer Center and the NAS facility at NASA Ames Research Center.

## REFERENCES

Abbott, I. H. & Doenhoff, A. E. von 1959 *Theory of Wing Sections*. Dover.

Bers, A. 1983 *Handbook of Plasma Physics*, I: *Basic Plasma Physics*. North-Holland.

Braslow, A. L., Maddalon, D. V., Bartlett, D. W., Wagner, R. D. & Collier Jr., F. S. 1990 Applied aspects of laminar-flow technology. In *Progress in Aeronautics and Astronautics*, Vol. 123 (ed. D. M. Bushnell & J. N. Hefner) pp. 47–78. AIAA.

Choudhari, M. 1994 Roughness-induced generation of crossflow vortices in three-dimensional boundary layers. *Theor. Comput. Fluid Dyn.* **6**, 1–30.

Choudhari, M. & Streett, C. 1990 Boundary layer receptivity phenomena in three-dimensional and high-speed boundary layers. *AIAA Paper* 90-5258.

Choudhari, M. & Streett, C. L. 1994 Theoretical prediction of boundary-layer receptivity. *AIAA Paper* 94-2223.

Collis, S. S. 1997 A computational investigation of receptivity in high-speed flow near a swept leading-edge. PhD thesis, Stanford University.

Conte, S. D. 1966 The numerical solution of linear boundary value problems. *SIAM Rev.* **8**, 309–321.

Cooke, J. C. 1950 The boundary layer of a class of infinite yawed cylinders. *Math. Proc. Camb. Phil. Soc.* **46**, 645–648.

Crouch, J. D. 1993 Receptivity of three-dimensional boundary layers. *AIAA Paper* 93-0074.

Crouch, J. D. 1994 Theoretical studies on the receptivity of boundary layers. *AIAA Paper* 94-2224.

Crouch, J. D. & Spalart, P. R. 1995 A study of non-parallel and nonlinear effects on the localized receptivity of boundary layers. *J. Fluid Mech.* **290**, 29–37.

Davis, R. T. 1972 Numerical solution of the Navier–Stokes equations for symmetric laminar incompressible flow past a parabola. *J. Fluid Mech.* **51**, 417–433.

Deyhle, H. & Bippes, H. 1996 Disturbance growth in an unstable three-dimensional boundary layer and its dependence on environmental conditions. *J. Fluid Mech.* **316**, 73–113.

Fasel, H. & Konzelmann, U. 1990 Non-parallel stability of a flat-plate boundary layer using the complete Navier–Stokes equations. *J. Fluid Mech.* **221**, 311–347.

Goldstein, M. E. 1985 Scattering of acoustic waves into Tollmien–Schlichting waves by small streamwise variations in surface geometry. *J. Fluid Mech.* **154**, 509–529.

Haynes, T. S. & Reed, H. L. 1996 Computations in nonlinear saturation of stationary crossflow vortices in a swept-wing boundary layer. *AIAA Paper* 96-0182.

Herbert, T. 1991 Boundary-layer transition—analysis and prediction revisited. *AIAA Paper* 91-0737.

Israeli, M. & Orszag, S. A. 1981 Approximation of radiation boundary condition. *J. Comput. Phys.* **41**, 115–135.

Ling, C.-H. & Reynolds, W. C. 1973 Non-parallel flow correction for the stability of shear flows. *J. Fluid Mech.* **59**, 571–591.

Malik, M. R. 1990 Stability theory for laminar flow control design. In *Viscous Drag Reduction in Boundary Layers, Progress in Aeronautics and Astronautics*, Vol. 123 (ed. D. M. Bushnell & J. N. Hefner) pp. 3–46. AIAA.

Malik, M. R. & Balakumar, P. 1993 Linear stability of three-dimensional boundary layers: Effects of curvature and non-parallelism. *AIAA Paper* 93-0079.

Malik, M. R. & Li, F. 1993 Transition studies for swept wing flows using PSE. *AIAA Paper* 93-0077.

Malik, M. R., Li, F. & Chang, C.-L. 1994 Cross-flow disturbances in three-dimensional boundary layers: non-linear deveopment, wave interaction and secondary instability. *J. Fluid Mech.* **268**, 1–36.

Masad, J. A. & Malik, M. R. 1994 Effects of body curvature and non-parallelism on the stability of flow over a swept cylinder. *Phys. Fluids* **6**, 2363–2379.

Morkovin, M. V. 1969 Bypass-transition research: issues and philosophy. *Tech. Rep.* AFFDL-TR-68-149. Air Force Flight Dynamics Laboritory, Wright–Paterson Air Force Base.

Poll, D. I. A. 1985 Some observations of the transition process on the windward face of a long yawed cylinder. *J. Fluid Mech.* **150**, 329–356.

Radeztsky Jr., R. H., Reibert, M. S. & Saric, W. S. 1993 Effect of micron-sized roughness on transition in swept-wing flows. *AIAA Paper* 93-0076.

Reibert, M. S., Saric, W. S., Carrillo Jr., R. B. & Chapman, K. L. 1996 Experiments in nonlinear saturation of stationary crossflow vortices in a swept-wing boundary layer. *AIAA Paper* 96-0184.

Reshotko, E. & Beckwith, I. E. 1958 *Compressible Laminar Boundary Layer over a Yawed Infinite Cylinder with Heat Transfer and Arbitrary Prandtl Number. NACA Tech. Rep.* 1379.

Ruban, A. I. 1984 On the generation of Tollmien–Schlichting waves by sound. *Fluid Dyn.* **19**, 709–717.

Saric, W. S. & Nayfeh, A. H. 1975 Nonparallel stability of boundary-layer flows. *Phys. Fluids* **18**, 945–950.

Sherman, F. S. 1990 *Viscous Flow*, pp. 644–658. McGraw-Hill.

Spalart, P. R. 1989 Direct numerical study of leading-edge contamination. In *Fluid Dynamics of Three-Dimensional Turbulent Shear Flows and Transition*, AGARD-CP-438.

Topham, D. R. 1965 A correlation of leading edge transition and heat transfer on swept cylinders in supersonic flow. *J. R. Aeronaut. Soc.* **69**, 49–52.

Van Dyke, M. 1963 Higher approximations in boundary-layer theory part 3. parabola in uniform stream. *J. Fluid Mech.* **19**, 145–159.

Zavol'skii, N. A., Reutov, V. P. & Ryboushkina, G. V. 1983 Generation of Tollmien–Schlichting waves via scattering of acoustic and vortex perturbations in boundary layer on wavy surface. *J. Appl. Mech. Tech. Phys.* **24**, 79–86.